



# Synthesis of $\text{WO}_3/\text{BiVO}_4$ photoanode using a reaction of bismuth nitrate with peroxovanadate on $\text{WO}_3$ film for efficient photoelectrocatalytic water splitting and organic pollutant degradation

Qingyi Zeng<sup>a</sup>, Jinhua Li<sup>a,\*</sup>, Linsen Li<sup>a</sup>, Jing Bai<sup>a</sup>, Ligang Xia<sup>a</sup>, Baoxue Zhou<sup>a,b,\*</sup>

<sup>a</sup> School of Environmental Science and Engineering, Shanghai Jiao Tong University, Shanghai 200240, China

<sup>b</sup> Key Laboratory of Thin Film and Microfabrication Technology, Ministry of Education, Shanghai 200240, PR China



## ARTICLE INFO

### Article history:

Received 3 January 2017

Received in revised form 18 May 2017

Accepted 25 May 2017

Available online 26 May 2017

### Keywords:

Photoelectrocatalysis

$\text{BiVO}_4$

$\text{WO}_3$

Water splitting

Organic pollutants

## ABSTRACT

In this work, we developed a novel, facile, cost-effective method based on a reaction of bismuth nitrate with peroxovanadate on  $\text{WO}_3$  nanoplate films to synthesize nanostructured  $\text{WO}_3/\text{BiVO}_4$  photoanodes, which prevented the introduction of structural defects in the  $\text{WO}_3$  substrates that occurs in conventional deposition-annealing (DA) methods, for highly efficient photoelectrocatalytic (PEC) water splitting and degradation of organic pollutants. The method is also versatile, allowing dopants such as Mo to be easily incorporated into  $\text{BiVO}_4$  structures to improve the charge-transfer properties. Both the amount of  $\text{BiVO}_4$  and doping level can be tailored by modifying the preparation conditions. The PEC performance of the optimized  $\text{WO}_3/\text{BiVO}_4$  photoanode was markedly improved with a photocurrent density of  $2.83 \text{ mA cm}^{-2}$ , which was 9.43 times that of a  $\text{BiVO}_4$  photoanode and 2.19 times that of a  $\text{WO}_3$  photoanode. A Mo-doped  $\text{WO}_3/\text{BiVO}_4$  ( $\text{WO}_3/\text{Mo-BiVO}_4$ ) photoanode exhibited a further enhanced photocurrent density of  $3.78 \text{ mA cm}^{-2}$ . Specifically, a cobalt-phosphate (Co-Pi) co-catalyst decorated  $\text{WO}_3/\text{Mo-BiVO}_4$  photoanode showed the highest photocurrent density of  $5.38 \text{ mA cm}^{-2}$ , which is comparable to the values of reported  $\text{WO}_3/\text{BiVO}_4$  photoanodes, with stoichiometric  $\text{H}_2$  ( $94.7 \mu\text{mol cm}^{-2} \text{ h}^{-1}$ ) and  $\text{O}_2$  ( $46.5 \mu\text{mol cm}^{-2} \text{ h}^{-1}$ ) evolution. Furthermore, the  $\text{WO}_3/\text{Mo-BiVO}_4$  photoanode exhibited efficient performance for PEC degradation of organic pollutants with rate constants of 0.683, 0.385, and  $1.05 \text{ h}^{-1}$  for tetracycline hydrochloride, phenol, and Congo red, respectively. Intensity-modulated photocurrent spectroscopy measurements indicated the  $\text{WO}_3/\text{BiVO}_4$  photoanode should contain fewer nanostructural defects than the  $\text{WO}_3/\text{BiVO}_4$  photoanode prepared using DA methods, possibly because the moderate preparation process avoids the harmful repeated heating-cooling process used in DA.

© 2017 Elsevier B.V. All rights reserved.

## 1. Introduction

The extensive use of fossil fuels has resulted in global environmental issues, such as global warming, acid rain, and etc. which threaten the subsistence of all species living on the earth. In addition, fossil fuels are a limited resource. In order to reduce fossil fuel consumption and at the same time address the associated environmental problems, the need to increase the utilization of clean energy, such as solar energy, has been widely acknowledged. Inspired by the pioneering work of Fujishima and Honda [1], a

photoelectrocatalytic (PEC) technique has been developed to solve these problems using sunlight to split water and degrade organic pollutants [2–9].

A critical component in the PEC technique is the photoelectrode, which should exhibit excellent visible-light response and charge-transport capacities to ensure efficient sunlight absorption and energy conversion [10–12]. The  $\text{WO}_3/\text{BiVO}_4$  heterostructure is one of the most attractive quasi-type II photoanode materials because  $\text{BiVO}_4$  serves as a good visible-light absorber ( $\sim 30\%$  sunlight) and  $\text{WO}_3$  functions as an efficient electron conductor ( $\sim 12 \text{ cm}^2 \text{ V}^{-1} \text{ s}^{-1}$ ) [13–23]. Several types of  $\text{WO}_3/\text{BiVO}_4$  nanostructures, such as compact nanofilms [15,16], mesoporous films [17,18] and array-structured films [19–23], have been synthesized for PEC applications. Although  $\text{WO}_3/\text{BiVO}_4$  heterostructured photoanodes were getting attention, very few attentions were devoted to the

\* Corresponding authors at: School of Environmental Science and Engineering, Shanghai Jiao Tong University, Shanghai 200240, China

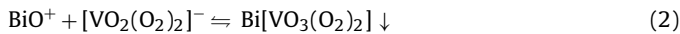
E-mail addresses: [lijinhua@sjtu.edu.cn](mailto:lijinhua@sjtu.edu.cn) (J. Li), [zhoubaoxue@sjtu.edu.cn](mailto:zhoubaoxue@sjtu.edu.cn) (B. Zhou).

fabrication methods of BiVO<sub>4</sub> on WO<sub>3</sub> films. For instance, the most widely used method in the reported works is called deposition-annealing (DA) method [14], which is mainly based on the following reaction (Eq. (1)).



The DA method is a simple and versatile way to prepare BiVO<sub>4</sub> layers on various substrates, which promotes the research of WO<sub>3</sub>/BiVO<sub>4</sub> photoanodes [15–21]. However, this method would increase crystal defects in the WO<sub>3</sub> substrates because of the thermal stress from the repeated heating-cooling process used to increase the amount of BiVO<sub>4</sub>, which may impair the charge-transport property of the WO<sub>3</sub>/BiVO<sub>4</sub> photoanode [14]. Furthermore, this method is not cost-effective because the BiVO<sub>4</sub> precursor of the mixed solution containing bismuth and vanadium sources is not stable for the slow sedimentation of BiVO<sub>4</sub> [18]. In this case, how to avoid the negative effect on WO<sub>3</sub> substrates, and developing a facile and cost-effective method to fabricate WO<sub>3</sub>/BiVO<sub>4</sub> photoanodes is highly desirable.

In this work, we proposed a new method to fabricate nanostructured WO<sub>3</sub>/BiVO<sub>4</sub> photoanodes based on the reaction of bismuth nitrate with peroxovanadate (Eq. (2)) on WO<sub>3</sub> nanoplate array films' surface for efficient PEC water splitting and organic pollutants degradation.



The amount of deposited BiVO<sub>4</sub> can be adjusted by spin-coating an alternative deposition of bismuth nitrate solution and peroxovanadate solution on the surface of WO<sub>3</sub> films, which avoids the repeated heat treatment performed during spin-coating in conventional DA methods. Furthermore, the stable separated precursors of bismuth nitrate and peroxovanadate solutions indicate that this method is more cost-effective than conventional DA methods. Following only once annealing process (Eq. (3)), the WO<sub>3</sub>/BiVO<sub>4</sub> photoanodes were obtained.



This method is also versatile, enabling dopants such as Mo to be easily incorporated into BiVO<sub>4</sub> structures. The doping level can be tailored by tuning the preparation conditions. The WO<sub>3</sub>/BiVO<sub>4</sub> photoanodes showed significantly improved PEC performance compared with the bare WO<sub>3</sub> photoanodes and single BiVO<sub>4</sub> photoanodes. The Mo-doped WO<sub>3</sub>/BiVO<sub>4</sub> (WO<sub>3</sub>/Mo-BiVO<sub>4</sub>) photoanodes exhibited further improved PEC performance for both water splitting and the degradation of organic pollutants. Particularly, the Co-Pi decorated WO<sub>3</sub>/Mo-BiVO<sub>4</sub> photoanode showed a photocurrent density of 5.38 mA cm<sup>-2</sup> at 1.23 V vs. RHE, corresponding to ~72% of the theoretically possible value for BiVO<sub>4</sub>, which is comparable to that of reported WO<sub>3</sub>/BiVO<sub>4</sub> photoanodes. Furthermore, the WO<sub>3</sub>/Mo-BiVO<sub>4</sub> photoanode exhibited degradation rate constants of 0.683, 0.385, and 1.05 h<sup>-1</sup> for PEC degradation of tetracycline hydrochloride, phenol, and Congo red, respectively. These results indicate that this alternative method enables facile, controllable, and cost-effective preparation of highly active WO<sub>3</sub>/BiVO<sub>4</sub> photoanodes for possible applications in efficient PEC water splitting and wastewater treatment.

## 2. Experimental

### 2.1. Preparation of WO<sub>3</sub> film

The WO<sub>3</sub> film was prepared via a simple wet chemical method based on a peroxotungstate reduction reaction [24]. The purchased fluorine-doped tin oxide (FTO) coated glass substrate (13 Ω cm<sup>-1</sup>) was cut into 3 × 3 cm<sup>2</sup> and washed ultrasonically in acetone and

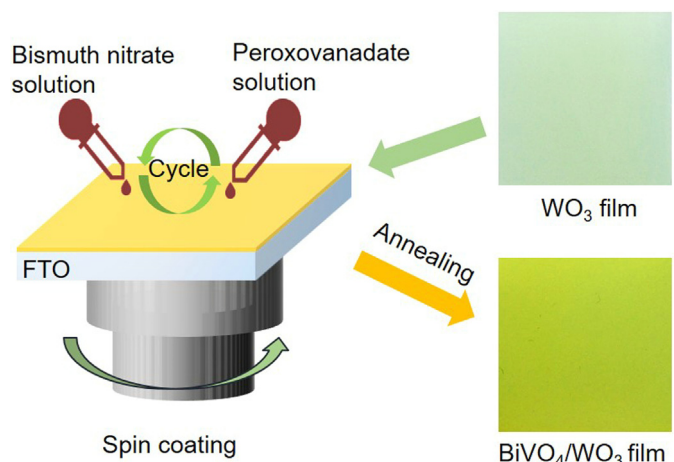


**Fig. 1.** Scheme of the preparation of BiVO<sub>4</sub>/WO<sub>3</sub> photoanodes.

deionized (DI) water for 30 min, sequentially. The precursor solution was prepared as follows: 0.6 g H<sub>2</sub>WO<sub>4</sub>, 0.28 g (NH<sub>4</sub>)<sub>2</sub>C<sub>2</sub>O<sub>4</sub>, 18 mL of HCl (37%) and 16 mL of H<sub>2</sub>O<sub>2</sub> (37%) were dissolved in 66 mL of DI water sequentially; then, 60 mL of ethanol was added to this solution under strong agitation to obtain the precursor solution. The FTO glass was dipped into this precursor solution with the FTO side down and then kept in a constant temperature bath at 85 °C for 3 h before being allowed to cool naturally. The as-prepared film was rinsed with plenty DI water and dried at 80 °C for 5 h, and finally annealed at 500 °C for 3 h to obtain the WO<sub>3</sub> film.

### 2.2. Preparation of WO<sub>3</sub>/BiVO<sub>4</sub> photoanodes

The WO<sub>3</sub>/BiVO<sub>4</sub> photoanodes were prepared using spin-coating processes based on the reaction of bismuth nitrate with peroxovanadate (Fig. 1). Before the preparation process, the bismuth nitrate solution was prepared by dissolving 2.43 g Bi(NO<sub>3</sub>)<sub>3</sub>·5H<sub>2</sub>O in 100 mL of 2 M acetic acid solution. For the peroxovanadate solution, 0.585 g NH<sub>4</sub>VO<sub>3</sub> was dissolved in 100 mL of 100 mM H<sub>2</sub>O<sub>2</sub> solution ultrasonically, resulting in a saffron-yellow solution (pH 7.4). In a typical preparation process, 0.5 mL of bismuth nitrate solution was coated on the WO<sub>3</sub> film (a retention time of 30 s) following with a spin rate of 2000 r.p.m. for 15 s, and then 0.5 mL of peroxovanadate solution was deposited on the film using the same spin-coating conditions. This process was considered one spin-coating cycle, and typically 15 cycles were used. Then, the film was rinsed with DI water and dried at 50 °C for 10 h before being annealed at 450 °C for 5 h to obtain the WO<sub>3</sub>/BiVO<sub>4</sub> photoanode. To prepare BiVO<sub>3</sub> photoanodes, the WO<sub>3</sub> film was replaced by the FTO glass, and 20 spin-coating cycles were used. For the WO<sub>3</sub>/Mo-BiVO<sub>4</sub> photoanodes, 0.017 g (NH<sub>4</sub>)<sub>6</sub>Mo<sub>7</sub>O<sub>24</sub> (2 atomic% of Mo/Bi) was added to the peroxovanadate solution, and 15 spin-coating cycles were used.

### 2.3. Deposition of Co-Pi co-catalyst

The deposition of Co-Pi co-catalyst was performed using a photo-assisted electro-deposition method in a three-electrode system with the WO<sub>3</sub>/Mo-BiVO<sub>4</sub> photoanode as the working electrode, Pt foil as the counter electrode, and a saturated calomel electrode (SCE) as the reference electrode. For the electrolyte, 0.1 M sodium phosphate buffer solution at pH 7 containing 0.5 mM Co(NO<sub>3</sub>)<sub>2</sub> was used. The deposition was performed at 0.1 V for 300 s under AM 1.5 illumination. After the deposition, the Co-Pi/WO<sub>3</sub>/Mo-BiVO<sub>4</sub> photoanode was rinsed with DI water and then dried at 50 °C for 1 h.

## 2.4. Characterization

The morphologies and microstructures of the samples were investigated using scanning electron microscopy (SEM, Sirion200, Philips, Netherlands) at an acceleration voltage of 5 kV. The crystal phase of the samples was characterized using X-ray diffraction (XRD, AXS-8 Advance, Bruker, Germany). Raman spectra were recorded on SENTERRA R200 system (Bruker, Germany) with a laser excitation of 532 nm. X-ray photoelectron spectroscopy (XPS) spectra were measured using an AXIS Ultra DLD (Kratos, Shimadzu, Japan) with non-chromatic Al K $\alpha$  radiation at 12 kV and 25 mA. The ultraviolet-visible (UV-vis) absorption spectra of the samples were obtained using a UV-vis photospectrometer (TU-1901, PGeneral Instrument Inc., China). The incident-photon-to-charge conversion efficiency (IPCE) was measured using a system operated with a monochromator (Zolix, China), 500-W xenon arc lamp, calibrated silicon photodetector, and power meter.

## 2.5. Photoelectrocatalytic properties

PEC tests were performed in a three-electrode system with a SCE as the reference electrode, Pt foil as the counter electrode, and the as-prepared photoanodes as the working electrode (front-side illumination) in an electrolyte consisting of 0.5 M K<sub>2</sub>SO<sub>4</sub> solution. The tests were controlled using an electrochemical workstation (CHI 660c, CH Instruments, Inc., USA). A 300-W Xe lamp (PerfectLight, China) with an AM 1.5 filter was used for light illumination (light density: 100 mW cm<sup>-2</sup>). The potentials were measured relative to the SCE and converted to the reversible hydrogen electrode (RHE) scale using the following equation:

$$E_{\text{RHE}} = E_{\text{SCE}} + 0.0591 \times \text{pH} + E^0_{\text{SCE}},$$

where  $E_{\text{RHE}}$  is the calculated potential vs. RHE,  $E_{\text{SCE}}$  is the measured potential, the pH is 7.1, and  $E^0_{\text{SCE}}$  is 0.2415 V at 25 °C.

The hydrogen and oxygen evolution were measured in a quartz device (LabSolar-IIAG, Perfect Light, China), which included a gas-collection system and reactor. This device was connected to a vacuum pump (2TW-6G, Tingwei, China), low-constant-temp bath (DC-2006, CNSHP, China), and gas chromatograph (GC; GC-2010plus, Shimadzu, Japan). Before water splitting, the quartz device was placed under vacuum using a vacuum pump to remove the dissolved gas of the electrolyte and the air in the device. The temperature of the low-constant-temp bath was -2 °C to prevent the water vapor from the electrolyte from entering the gas-collection system. During the test, a certain amount of gas in the gas-collection system was sent to the GC system to analyze the amount of H<sub>2</sub> and O<sub>2</sub> after certain intervals.

Intensity-modulated photocurrent spectroscopy (IMPS) was performed using an electrochemical workstation (Zennium; effect-Elektrik, Germany) equipped with a controlled intensity-modulated photospectroscopy set-up (CIMPS, PP211), following a three-electrode configuration, with the WO<sub>3</sub>/BiVO<sub>4</sub> photoanodes as the working electrode, Pt foil as the counter electrode, and a SCE as the reference electrode with a 0.5 M K<sub>2</sub>SO<sub>4</sub> electrolyte. A white-light lamp (WLC02; Zahner-Elektrik) was used as the light source. Modulated light in the frequency range of 0.1–10 kHz superimposed on a steady DC light intensity of 80 mW cm<sup>-2</sup> was applied. The bias potential applied at the working electrode was 0.6 V vs. SCE.

The organic pollutant degradation experiment was performed under the following conditions: moderate stirring, 0.1 M sodium sulfate as the supporting electrolyte containing 10 mg L<sup>-1</sup> tetracycline hydrochloride (or phenol or Congo red), 25 mL of reaction solution, and a 1 cm<sup>2</sup> illumination area for the photoanodes. The degradation rates of tetracycline hydrochloride and Congo

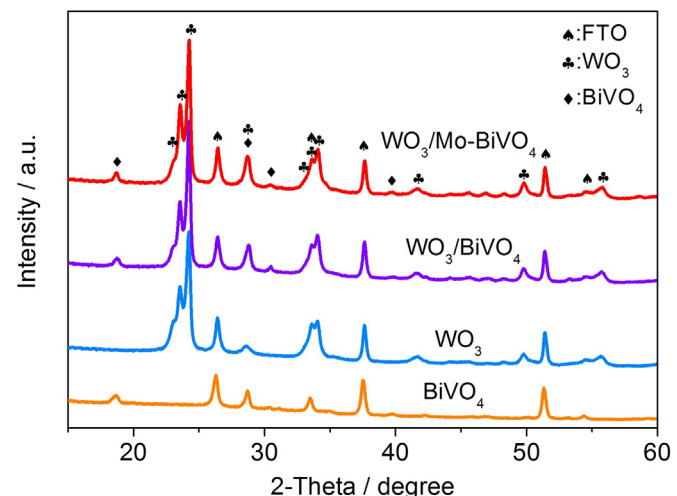


**Fig. 2.** XRD patterns of the as prepared photoanodes.

red were analyzed with a spectrophotometer (TU-1901, PGeneral Instrument Inc., China) at wavelengths of 357 and 488 nm, respectively. The degradation rate of phenol was monitored using gas chromatogram (GC-14B) analysis. All the measurements were performed under ambient conditions.

## 3. Results and discussion

### 3.1. Synthesis and characterization

In this study, we developed an alternative technique for the synthesis of WO<sub>3</sub>/BiVO<sub>4</sub> photoanodes based on the reaction of bismuth nitrate with peroxovanadate on nanostructured WO<sub>3</sub> films (Fig. 1). Compared with the sluggish reaction between Bi(NO<sub>3</sub>)<sub>3</sub> solution and NH<sub>4</sub>VO<sub>3</sub> solution, the Bi(NO<sub>3</sub>)<sub>3</sub> solution can react with peroxovanadate solution immediately to produce orange precipitation bismuth peroxovanadate (Eq. (2)), which is critical to the new developed method (Fig. S1). As observed in Fig. 1, both the WO<sub>3</sub> and WO<sub>3</sub>/BiVO<sub>4</sub> photoanodes were uniform. The color of WO<sub>3</sub> film was light olive, and the WO<sub>3</sub>/BiVO<sub>4</sub> photoanode was yellow-green. This method clearly avoids the repeated heating-cooling process used in conventional deposition-annealing (DA) methods [14–22], which could eliminate the formation of defect sites in WO<sub>3</sub> substrates, resulting in a more efficient photoelectrocatalytic (PEC) performance. This versatile method can also be used to dope metal elements (such as Mo) into BiVO<sub>4</sub>. More details are provided in the Supporting Information. Based on the PEC tests, as shown in Fig. S3 and Fig. S4, the optimum number of spin-coating cycles and doping amount of Mo were 15 and 2 atomic%, respectively. Therefore, without otherwise specified, the mentioned WO<sub>3</sub>/BiVO<sub>4</sub> photoanode and Mo-doped BiVO<sub>4</sub> decorated WO<sub>3</sub> (WO<sub>3</sub>/Mo-BiVO<sub>4</sub>) photoanode in the following text were prepared under these optimized conditions.

The crystallographic features of the as prepared photoanodes were investigated using X-ray diffraction (XRD), and the results are presented in Fig. 2. For the BiVO<sub>4</sub> photoanode prepared on the FTO substrate, the diffraction peaks at 18.5° and 29.4° are attributed to monoclinic BiVO<sub>4</sub> (JCPDS 14-0688), which is the most active structure for photocatalysis [25]. For the WO<sub>3</sub> photoanode, the diffraction peaks at 23.3°, 23.8°, and 24.6° correspond to (002), (020), and (200) planes for monoclinic WO<sub>3</sub> (JCPDS 43-1035), which is known to show the highest photocatalytic activity among other crystal phases [26]. The intensified (200) diffraction peak indicates that the nanostructured WO<sub>3</sub> film has a preferential orientation of [200]. The WO<sub>3</sub>/BiVO<sub>4</sub> and WO<sub>3</sub>/Mo-BiVO<sub>4</sub> photoanodes have

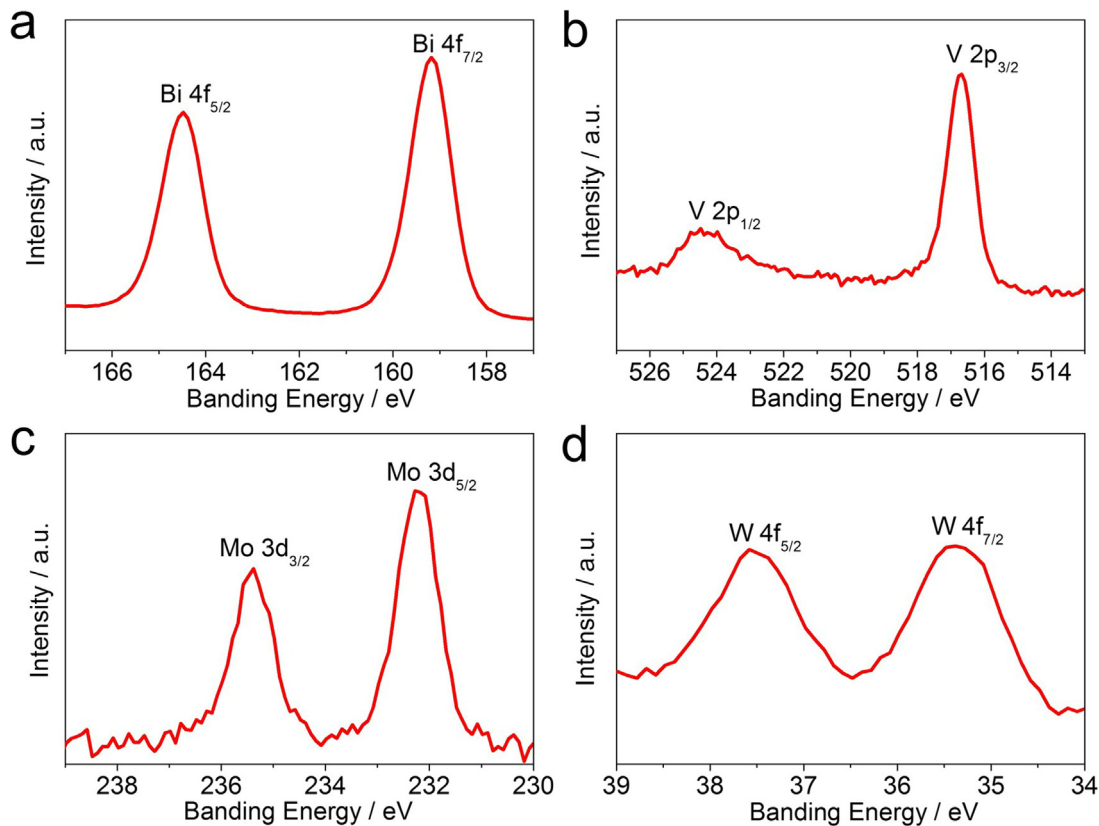


**Fig. 3.** XPS analysis of the  $\text{WO}_3/\text{Mo}-\text{BiVO}_4$  photoanode: (a)  $\text{Bi } 4\text{f}$ , (b)  $\text{V } 2\text{p}$ , (c)  $\text{Mo } 3\text{d}$ , and (d)  $\text{W } 4\text{f}$  core level spectra.

similar XRD patterns, indicating that both photoanodes consist of monoclinic  $\text{WO}_3$  and monoclinic  $\text{BiVO}_4$ . No evidence for the doping of Mo is observed, which should be due to its small amount (2 atomic%). The Raman spectra confirm the existences of pure monoclinic  $\text{WO}_3$  and monoclinic  $\text{BiVO}_4$  in the as prepared photoanodes, and indicate the cooperation of Mo into  $\text{BiVO}_4$  for the  $\text{WO}_3/\text{Mo}-\text{BiVO}_4$  photoanode (Fig. S5).

To better detect the Mo species in the  $\text{WO}_3/\text{Mo}-\text{BiVO}_4$  photoanode, X-ray photoelectron spectroscopy (XPS) spectra of the  $\text{WO}_3/\text{Mo}-\text{BiVO}_4$  photoanode were surveyed (Fig. S6), and high-resolution XPS spectra of the  $\text{Bi } 4\text{f}$ ,  $\text{V } 2\text{p}$ ,  $\text{Mo } 3\text{d}$ , and  $\text{W } 4\text{f}$  regions on the surface of the  $\text{WO}_3/\text{Mo}-\text{BiVO}_4$  photoanode is shown in Fig. 3. The binding energy peaks at 159.3 and 164.5 eV (Fig. 3a) are ascribed to  $\text{Bi } 4\text{f}_{7/2}$  and  $\text{Bi } 4\text{f}_{5/2}$  states, which is consistent with the results from  $\text{Bi}^{3+}$  [27]. The peaks at 516.8 and 524.6 eV (Fig. 3b) are assigned to the  $\text{V } 2\text{p}_{3/2}$  and  $\text{V } 2\text{p}_{1/2}$  states of the tetrahedral  $\text{VO}_4^{3-}$  group, respectively. The binding energy peaks of  $\text{Mo } 3\text{d}$  are detected at 232.4 and 235.5 eV which are attributed to  $\text{Mo } 3\text{d}_{5/2}$  and  $\text{Mo } 3\text{d}_{3/2}$  signals of  $\text{Mo}^{6+}$  oxidation state, respectively [28]. This finding indicates that the Mo atoms are mainly present in the lattice as  $\text{Mo}^{6+}$  at V sites in  $\text{BiVO}_4$  [29]. A trace of  $\text{W}^{6+}$  was also detected at binding energies of 35.5 and 37.6 eV (Fig. 3d), which are attributed to  $\text{W } 4\text{f}_{7/2}$  and  $\text{W } 4\text{f}_{5/2}$ , respectively, and result from the porous morphology of the  $\text{BiVO}_4$  layer [30].

The morphology and nanostructure of the as-prepared photoanodes were examined using scanning electron microscopy (SEM). As shown in Fig. 4a, the  $\text{WO}_3$  photoanode exhibited a plate-like morphology with quasi-vertically oriented nanoplate arrays and a thickness of ~870 nm. The thickness of the  $\text{WO}_3$  nanoplates was 60–110 nm. The  $\text{WO}_3$  nanoplate array directly coated on the FTO substrate provides a large surface area to load more  $\text{BiVO}_4$  as well as a good charge-transfer channel, therefore improving the light absorption and charge-transport properties of the photoanodes.

For the  $\text{BiVO}_4$  photoanode (Fig. 4b), a mesoporous structure with a relatively plane surface and a thickness of 250 nm was observed. The  $\text{WO}_3/\text{BiVO}_4$  photoanode showed a porous morphology with nanoporous  $\text{BiVO}_4$  coated  $\text{WO}_3$  nanoplates and a film thickness of 980 nm (Fig. 4c). The  $\text{WO}_3/\text{Mo}-\text{BiVO}_4$  photoanode possessed a similar nanostructure, which suggests that doping with Mo does not change the morphology of the  $\text{BiVO}_4$  layer (Fig. 4c). Both the  $\text{WO}_3/\text{BiVO}_4$  and  $\text{WO}_3/\text{Mo}-\text{BiVO}_4$  photoanodes exhibited fantastic porous nanostructures with increased surface area for PEC reactions at the photoanode/electrolyte interface.

The optical absorption behaviors of the as-prepared films were investigated using UV-vis absorbance spectroscopy, and the results are presented in Fig. 5. The  $\text{WO}_3$  photoanode exhibited an absorption edge of ~475 nm. For the  $\text{BiVO}_4$  photoanode, the onset of light absorption was approximately 510 nm. The  $\text{WO}_3/\text{BiVO}_4$  photoanode also exhibited an absorption edge of ~510 nm, which indicates that the light absorption range of  $\text{WO}_3$  was improved by coupling with  $\text{BiVO}_4$ , which has a smaller band gap energy [15]. After doping with Mo, the  $\text{WO}_3/\text{Mo}-\text{BiVO}_4$  photoanode exhibited similar absorption behavior as the  $\text{WO}_3/\text{BiVO}_4$  photoanode, suggesting that the band gap energy of  $\text{BiVO}_4$  is not noticeably affected by doping with 2 atomic% Mo; this finding was consistent with previously reported experimental results [22]. These results indicate that both the  $\text{WO}_3/\text{BiVO}_4$  and  $\text{WO}_3/\text{Mo}-\text{BiVO}_4$  photoanodes possessed good visible-light absorption capacities.

### 3.2. PEC measurements

Chopped linear sweep voltammetry (LSV) plots of the as-prepared photoanodes are presented in Fig. 6a. The photocurrent density ( $J$ ) values of the  $\text{BiVO}_4$  and  $\text{WO}_3$  photoanodes were 0.30 and  $1.29 \text{ mA cm}^{-2}$  at 1.23 V vs. RHE, respectively. After the  $\text{WO}_3$  nanoplate film was decorated with the  $\text{BiVO}_4$  layer, the  $\text{WO}_3/\text{BiVO}_4$

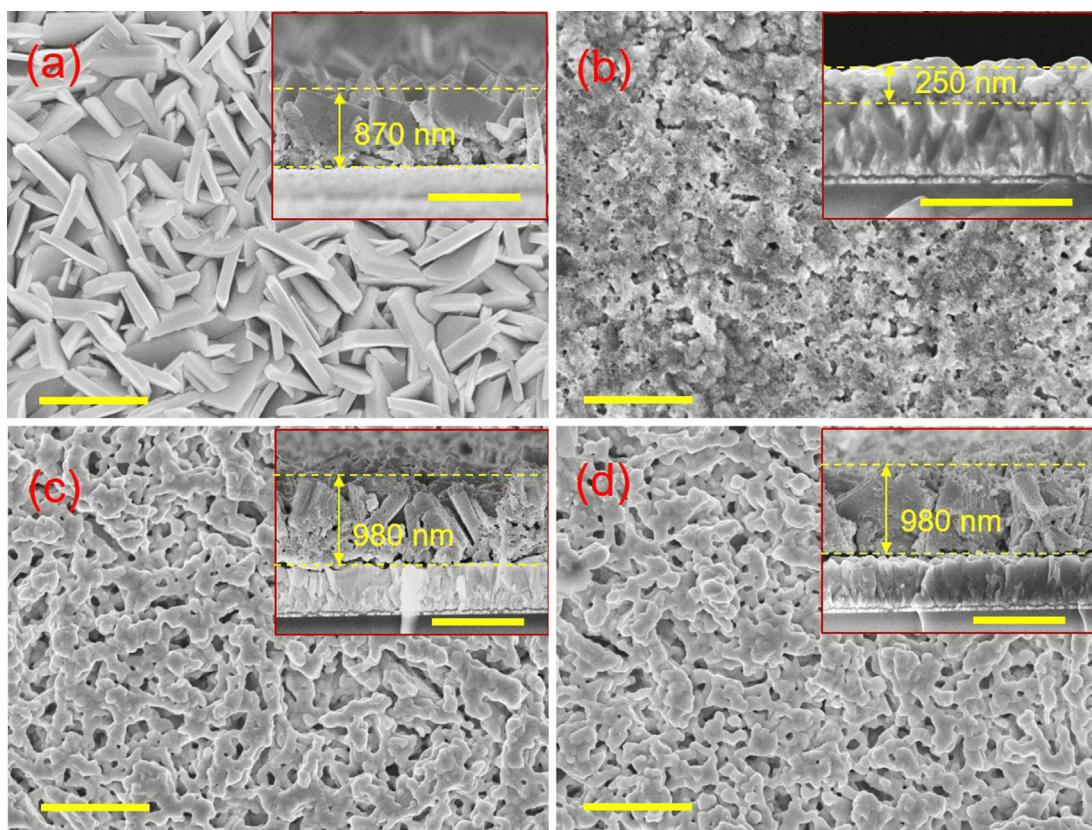


**Fig. 4.** SEM images of the (a) WO<sub>3</sub>, (b) BiVO<sub>4</sub>, (c) WO<sub>3</sub>/BiVO<sub>4</sub>, and (d) WO<sub>3</sub>/Mo-BiVO<sub>4</sub> photoanodes. The inserts are the corresponding cross-sectional SEM images. All the scale bars are 1  $\mu\text{m}$ .

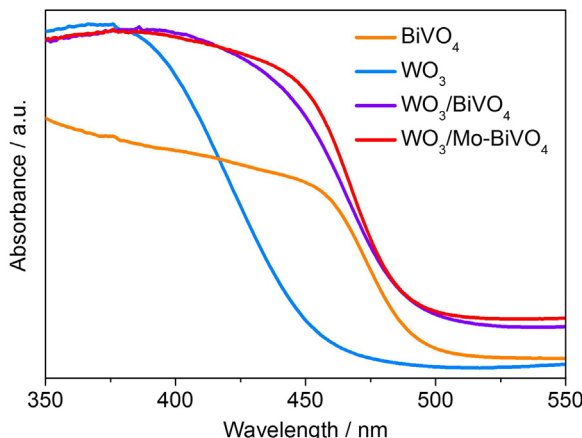


**Fig. 5.** UV-vis absorbance spectra of the as-prepared photoanodes.

photoanode exhibited a noticeable improvement in photocurrent response with a  $J$  of  $2.83 \text{ mA cm}^{-2}$  at  $1.23 \text{ V}$  vs. RHE, which is 9.43 times that of the BiVO<sub>4</sub> photoanode and 2.19 times that of the WO<sub>3</sub> photoanode. After doping Mo into the BiVO<sub>4</sub> layer, the WO<sub>3</sub>/Mo-BiVO<sub>4</sub> photoanode exhibited a further enhanced  $J$  of  $3.78 \text{ mA cm}^{-2}$  at  $1.23 \text{ V}$  vs. RHE, which is 133.6% of that of the WO<sub>3</sub>/BiVO<sub>4</sub> photoanode, suggesting much more efficient charge separation and collection in the WO<sub>3</sub>/Mo-BiVO<sub>4</sub> photoanode.

The incident-photon-to-current efficiency (IPCE) behaviors of these photoanodes tested at  $1.23 \text{ V}$  vs. RHE are presented in Fig. 6b. The as-prepared photoanodes exhibited IPCE responses in wavelength ranges roughly consistent with their light absorption spectra (Fig. 5). The BiVO<sub>4</sub> photoanode showed the lowest IPCE, with values lower than 10% in the entire light-response region. For the

WO<sub>3</sub> photoanode, the IPCE response is much higher than that of the BiVO<sub>4</sub> photoanode, which may result from the better charge transport property of WO<sub>3</sub>. Although WO<sub>3</sub> does not show a light response in the range of  $460$ – $520 \text{ nm}$ , both the WO<sub>3</sub>/BiVO<sub>4</sub> and WO<sub>3</sub>/Mo-BiVO<sub>4</sub> photoanodes exhibit efficient IPCE performances in this region, which can be due to the suitable thermodynamic energy band structure of heterostructured BiVO<sub>4</sub>/WO<sub>3</sub> inducing rapid transfer of photogenerated electrons in BiVO<sub>4</sub> to WO<sub>3</sub> [20–22]. These results demonstrate that the combination of BiVO<sub>4</sub> and WO<sub>3</sub> enables the resulting heterostructured photoanode to boost the strong photoresponse of BiVO<sub>4</sub> and charge-transport properties of WO<sub>3</sub> while completely eliminating the disadvantages including poor charge separation efficiency of BiVO<sub>4</sub> and weak photoresponse of WO<sub>3</sub>.

To further improve the water splitting efficiency, cobalt-phosphate (Co-Pi) co-catalyst, which is reported to be an efficient co-catalyst to facilitate oxygen evolution in water oxidation [31–33], is deposited on the WO<sub>3</sub>/Mo-BiVO<sub>4</sub> (Co-Pi/WO<sub>3</sub>/Mo-BiVO<sub>4</sub>) photoanode using photo-assisted electrodeposition. The energy-dispersive X-ray spectroscopy (EDX) results of the Co-Pi/WO<sub>3</sub>/Mo-BiVO<sub>4</sub> photoanode presented in Fig. S8 indicate that the Co-Pi/WO<sub>3</sub>/Mo-BiVO<sub>4</sub> photoanode consists of W, Bi, V, O, Mo, Co, and Pi and that the Co-Pi co-catalyst is decorated uniformly on the photoanode. As observed in Fig. 6a, the water splitting current density is noticeably enhanced after decorating the photoanode with the Co-Pi co-catalyst. The enhancement of the photocurrent density is particularly apparent at lower bias potentials, such as  $0.5$ – $1.2 \text{ V}$  vs. RHE, which indicates that the consumption of photogenerated holes for water oxidation is the bottleneck of PEC water splitting at a relatively lower potential. The Co-Pi/WO<sub>3</sub>/Mo-BiVO<sub>4</sub> photoanode exhibits the highest photocurrent density of  $5.38 \text{ mA cm}^{-2}$  at  $1.23 \text{ V}$  vs. RHE, corresponding

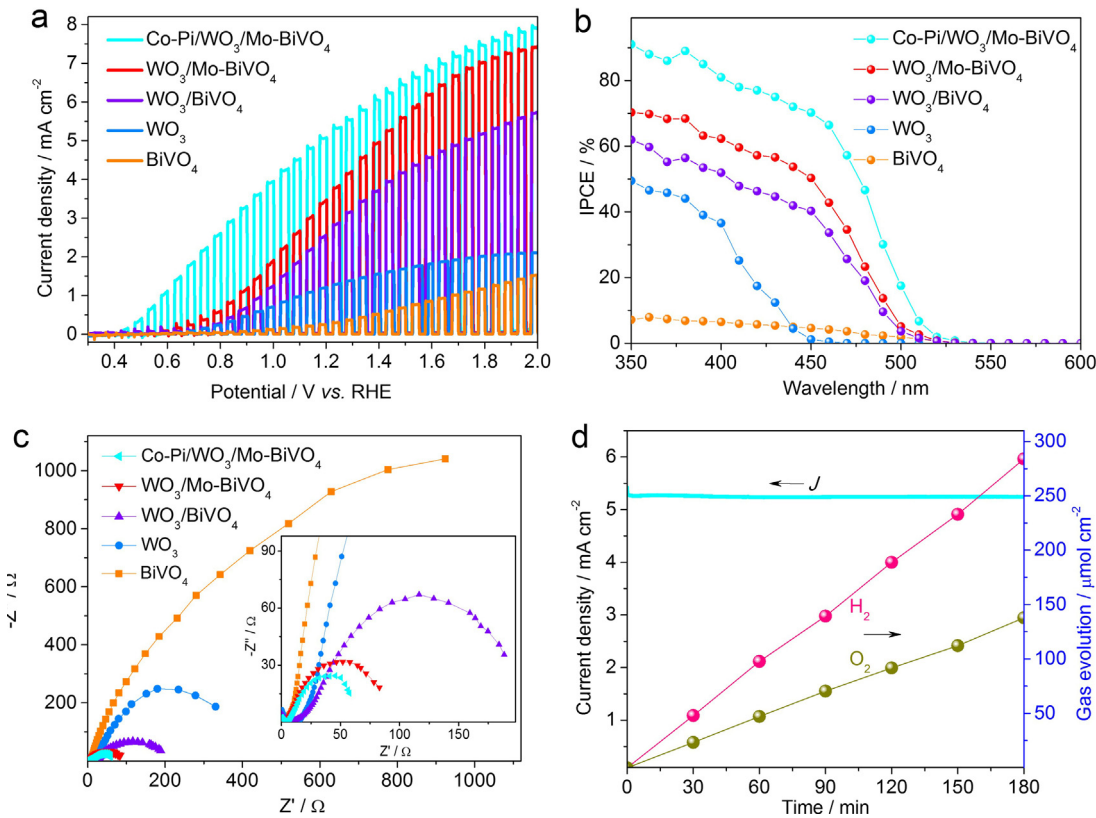


**Fig. 6.** (a) Chopped LSV plots, (b) IPCE curves (at 1.23 V vs RHE), and (c) Nyquist plots (at 1.23 V vs RHE) of the as prepared photoanodes. (d) The  $J$ - $t$  curve and water splitting performance of Co-Pi/WO<sub>3</sub>/Mo-BiVO<sub>4</sub> tested at 1.23 V vs RHE in 0.5 M K<sub>2</sub>SO<sub>4</sub> electrolyte under AM 1.5 illumination.

to ~72% of the theoretically possible value for BiVO<sub>4</sub> [23], which is 1.42 times that of the WO<sub>3</sub>/Mo-BiVO<sub>4</sub> photoanode. This value is comparable to reported values for WO<sub>3</sub>/BiVO<sub>4</sub> photoanodes [15–22]. Furthermore, the Co-Pi/WO<sub>3</sub>/Mo-BiVO<sub>4</sub> photoanode possesses the highest IPCE response among the prepared photoanodes (Fig. 6b). The IPCE values of the Co-Pi/WO<sub>3</sub>/Mo-BiVO<sub>4</sub> photoanode reach 91% at 350 nm and 80% at 400 nm and are higher than 70% in the range of 350–450 nm, which represent increases of approximately 20% compared with the WO<sub>3</sub>/Mo-BiVO<sub>4</sub> photoanode. These results indicate that the Co-Pi co-catalyst can facilitate the conversion of absorbed photons into photocurrents.

The photocurrent density and IPCE value of the as prepared photoanodes are further enhanced at a relatively high bias potential of 2.0 V vs. RHE because of the facilitated separation of electron/hole pairs in the photoanode (Fig. 6a and Fig. S9a). For example, the photocurrent density of Co-Pi/WO<sub>3</sub>/Mo-BiVO<sub>4</sub> photoanode increases to 7.89 mA cm<sup>-2</sup> at 2.0 V vs. RHE, which is 146% of the value at 1.23 V vs. RHE. The IPCE value of Co-Pi/WO<sub>3</sub>/Mo-BiVO<sub>4</sub> photoanode increases from 91% to 96% at 350 nm, while it increases from 17.5% to 33.4% at 500 nm, i.e. the utilization of the visible light becomes more efficient at 2.0 V vs. RHE. Therefore, the notably increased photocurrent density at 2.0 V vs. RHE can be mainly attributed to the improved IPCE value near the absorption edge, because the volcanic AM 1.5 solar spectrum has intense light intensity in the range of 480–580 nm (Fig. S9b).

To understand the charge-transfer properties of these photoanodes in PEC water splitting, electrochemical impedance spectroscopy (EIS) was performed in 0.5 M K<sub>2</sub>SO<sub>4</sub> electrolyte at 1.23 V vs. RHE under AM 1.5 illumination (Fig. 6c). The largest arc diameter of the BiVO<sub>4</sub> photoanode indicates its poor charge-transfer capacity for water splitting. The charge-transfer capacity of the WO<sub>3</sub> photoanode was better than that of the BiVO<sub>4</sub> photoanode for its smaller arc diameter. The charge-transfer capacity

of the WO<sub>3</sub>/BiVO<sub>4</sub> photoanode was remarkably enhanced when compared with those of BiVO<sub>4</sub> and WO<sub>3</sub>, which contributed to its higher PEC performance. The EIS results also reveal that Mo-doping increases the charge-transfer capacity of the WO<sub>3</sub>/Mo-BiVO<sub>4</sub> photoanode. However, the Co-Pi/WO<sub>3</sub>/Mo-BiVO<sub>4</sub> photoanode showed the highest charge-transfer capacity among these photoanodes.

The PEC water splitting performance of the Co-Pi/WO<sub>3</sub>/Mo-BiVO<sub>4</sub> photoanode was surveyed in 0.5 M K<sub>2</sub>SO<sub>4</sub> electrolyte at 1.23 V vs. RHE under AM 1.5 illumination (Fig. 6d). During the 180-min test, the H<sub>2</sub> and O<sub>2</sub> evolved in a stoichiometric ratio with generation rates of 94.7 and 46.5  $\mu\text{mol cm}^{-2} \text{ h}^{-1}$ , respectively, and an average water splitting current of approximately 5.24 mA cm<sup>-2</sup>. The calculated faradaic efficiencies were 96.9% and 94.1% for H<sub>2</sub> and O<sub>2</sub>, respectively, which are typical values for PEC water splitting with a monolithic electrolyte system, where the dissolved O<sub>2</sub> can undergo a partial back reaction at the Pt counter electrode [22]. This result indicates that the Co-Pi/WO<sub>3</sub>/Mo-BiVO<sub>4</sub> photoanode shows a great potential to split water into hydrogen and oxygen using solar energy.

To evaluate the advantages of this work compared with conventional DA methods, we prepared WO<sub>3</sub>/BiVO<sub>4</sub> photoanodes using a typical DA method [17] (Fig. S7a; in order to facilitate the distinction, they are described as DA-WO<sub>3</sub>/BiVO<sub>4</sub> photoanodes). The LSV test results (Fig. S7b) indicate that the photocurrent density of the WO<sub>3</sub>/BiVO<sub>4</sub> photoanode was 1.2 times that of the optimized DA-WO<sub>3</sub>/BiVO<sub>4</sub> photoanode (2.35 mA cm<sup>-2</sup> at 1.23 V vs RHE). Intensity-modulated photocurrent spectroscopy (IMPS) was further applied to measure the majority charge carrier transit time ( $\tau_d$ ) in these two photoanodes. IMPS is a powerful, nondestructive technique for characterization of the photogenerated carrier transportation and recombination/relaxation information in a photoelectrode [34–36]. The transit time ( $\tau_d$ ), the average time needed for the photogenerated charges (i.e., electrons) to reach the back

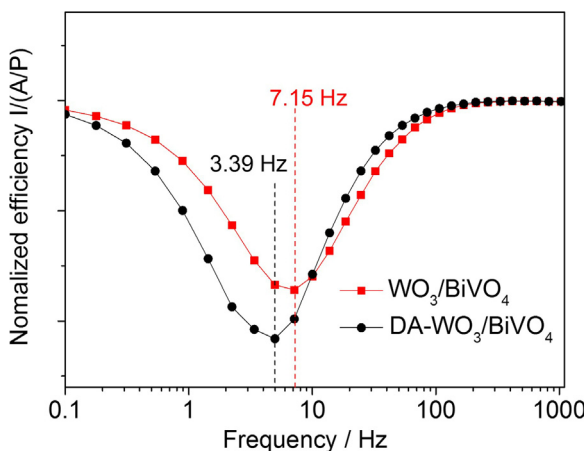


**Fig. 7.** The IMPS test results for  $\text{WO}_3/\text{BiVO}_4$  and DA- $\text{WO}_3/\text{BiVO}_4$  photoanodes.

contact (i.e., FTO substrate), can be estimated using  $\tau_d = (2\pi f_{min})^{-1}$ , where  $f_{min}$  is the frequency at the minimal value in the IMPS plot [34]. Based on the  $f_{min}$  value in Fig. 7, the calculated  $\tau_d$  values of the  $\text{WO}_3/\text{BiVO}_4$  and DA- $\text{WO}_3/\text{BiVO}_4$  photoanodes were 22.27 and 46.97 ms, respectively. The  $\tau_d$  value of the  $\text{WO}_3/\text{BiVO}_4$  photoanode was less than half of that of the DA- $\text{WO}_3/\text{BiVO}_4$  photoanode, indicating that the photogenerated charges more readily reached the back contact in the  $\text{WO}_3/\text{BiVO}_4$  photoanode than in the DA- $\text{WO}_3/\text{BiVO}_4$  photoanode. Because the nanostructured defects in the photoanode may generate a large number of crystal boundaries, which impede charge transport, the IMPS results indicate that the  $\text{WO}_3/\text{BiVO}_4$  photoanodes prepared in the current study should possess fewer nanostructural defects than the DA- $\text{WO}_3/\text{BiVO}_4$  photoanodes [35]. This difference could be due to the moderate preparation process based on the reaction of bismuth nitrate with peroxovanadate on  $\text{WO}_3$  films used in the present study; this process avoids the harmful repeated heating–cooling process used in conventional DA methods, which could lead to the higher photocurrent density. This result indicates that the method developed in this work is a promising alternative technique to prepare highly active  $\text{WO}_3/\text{BiVO}_4$  photoanodes for PEC applications.

### 3.3. Degradation of organic pollutants

Tetracycline hydrochloride is a widely used broad-spectrum antibiotic which is toxic and bio-refractory [37]. Its release into the water body is harmful to the eco-system and can cause persistent damage. Therefore, tetracycline hydrochloride was selected as one of the model substrates to evaluate the degradation efficiency of the as prepared photoanodes under AM 1.5 illumination. As shown in Fig. 8a, the direct photolysis of tetracycline hydrochloride was clearly much slower than the PEC processes, resulting in a removal ratio of only 8.2% after 3 h. Under the PEC conditions, the removal ratio for tetracycline hydrochloride with the  $\text{BiVO}_4$  photoanode was the lowest at only 22.1% after 3 h. The  $\text{WO}_3$  photoanode showed a removal ratio of 45.9%, while the heterostructured  $\text{WO}_3/\text{BiVO}_4$  photoanode showed significant improved removal ratio of 76.1%, which is approximately 1.66 and 3.44 times that of the  $\text{WO}_3$  and  $\text{BiVO}_4$  photoanodes, respectively. After doping with Mo, the  $\text{WO}_3/\text{Mo-BiVO}_4$  photoanode exhibited a further increased removal ratio of 85.6%, which is approximately 112% of that of the  $\text{WO}_3/\text{BiVO}_4$  photoanode. As shown in Fig. 8b, the ranking of the rate constant  $k$  of various processes was  $\text{WO}_3/\text{Mo-BiVO}_4$  ( $0.683 \text{ h}^{-1}$ ) >  $\text{WO}_3/\text{BiVO}_4$  ( $0.485 \text{ h}^{-1}$ ) >  $\text{WO}_3$  ( $0.226 \text{ h}^{-1}$ ) >  $\text{BiVO}_4$  ( $0.105 \text{ h}^{-1}$ ) > photolysis ( $0.039 \text{ h}^{-1}$ ). This result indicates that the  $\text{WO}_3/\text{Mo-BiVO}_4$  photoanode exhibited the best performance for PEC degradation of organics.

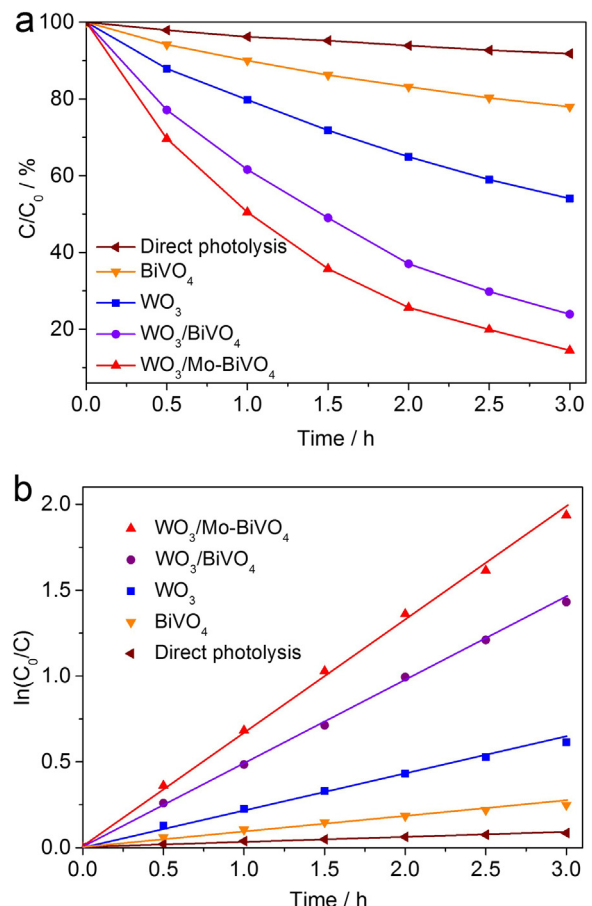


**Fig. 8.** (a) Degradation of tetracycline hydrochloride by direct photolysis, and using various photoanodes at a bias potential of 1 V vs SCE under AM 1.5 illumination. (b) Corresponding kinetic curves.

The performance of the  $\text{WO}_3/\text{Mo-BiVO}_4$  photoanode for PEC degradation of organics was further investigated using phenol and Congo red as model substrates. Phenol is a typical phenolic compound that is widely used in preservatives, herbicides, and pesticides [38]. It is highly toxic, persistent, and biorecalcitrant and can directly threaten the ecosystem and human health when discharged into ground and surface water. Congo red is a typical azo dye, which is widely used in textile industries, exhibits high toxicity, and can accumulate in the environment because of the release of industrial wastewater [39]. As observed in Fig. 9, the photolysis of phenol is much more difficult than that of Congo red. However, the removal ratios of phenol and Congo red were remarkably enhanced under the PEC process of the  $\text{WO}_3/\text{Mo-BiVO}_4$  photoanode; ~71.5% of the phenol and ~94.8% of the Congo red were removed after 3 h. The rate constant was  $\sim 0.385 \text{ h}^{-1}$  for phenol and  $\sim 1.05 \text{ h}^{-1}$  for Congo red. The different degradation efficiencies between the various organic matters can be attributed to their different molecular structures [40,41]. These results demonstrate that the  $\text{WO}_3/\text{Mo-BiVO}_4$  photoanode can be used in efficient wastewater treatment. The repeat uses of the  $\text{WO}_3/\text{Mo-BiVO}_4$  photoanode for PEC degradation of tetracycline hydrochloride (Fig. S10) further indicated that the  $\text{WO}_3/\text{Mo-BiVO}_4$  photoanode possesses excellent stability in PEC wastewater treatment.

Although  $\text{BiVO}_4$  has a wider light absorption range than  $\text{WO}_3$  (Fig. 5), it suffers from a poor charge-transport capacity (carrier diffusion length  $\sim 70 \text{ nm}$ ) [42] and sluggish surface reaction kinetics, which result in a severe recombination of electron-hole pairs [43,44]. It is reported that  $\text{BiVO}_4$  has more negative conduction band edge (CB) and valence band edge (VB) than  $\text{WO}_3$

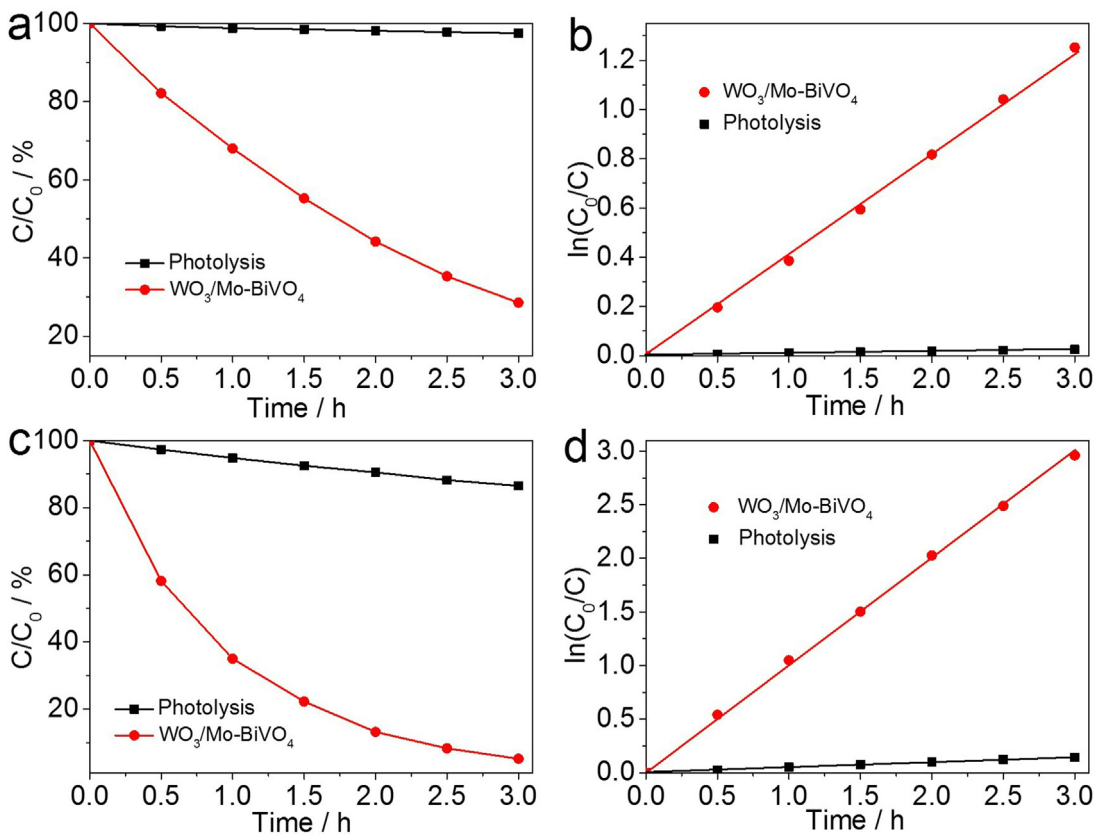


**Fig. 9.** Degradation of (a) phenol and (c) Congo red and (b, d) corresponding kinetic curves using direct photolysis and the  $\text{WO}_3/\text{Mo-BiVO}_4$  photoanode at a bias potential of 1 V vs. SCE under AM 1.5 illumination.

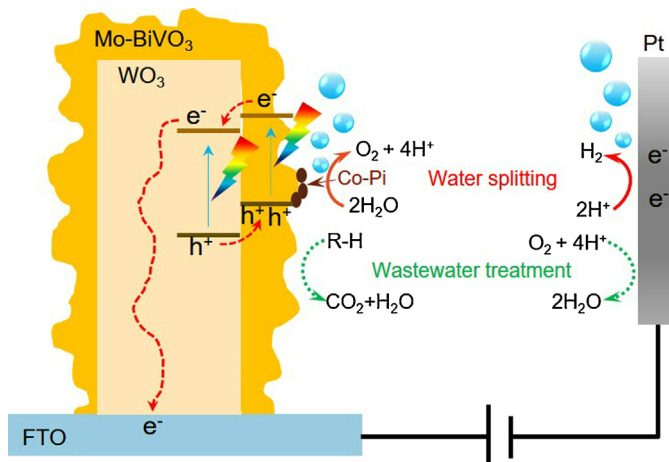


**Fig. 10.** Possible mechanisms for PEC water splitting by  $\text{Co-Pi}/\text{WO}_3/\text{Mo-BiVO}_4$  (red solid arrow) or degradation of organic pollutants by  $\text{WO}_3/\text{Mo-BiVO}_4$  (green dot arrow).

[15,45]. Therefore, the heterostructure of  $\text{WO}_3/\text{BiVO}_4$  is favorable for both the transport of photogenerated electrons from the CB of  $\text{BiVO}_4$  to that of  $\text{WO}_3$  and of photogenerated holes from the VB of  $\text{WO}_3$  to that of  $\text{BiVO}_4$  because of the quasi type-II interfacial band structure (Fig. 10). This behavior in turn suppresses the recombination of electron-hole pairs because of the strong thermodynamic effect. Furthermore, the good charge-transport property of  $\text{WO}_3$  nanoplates ensures the photogenerated electrons transfer to the FTO substrate and further to the Pt cathode [46,47]. Therefore, the  $\text{WO}_3/\text{BiVO}_4$  photoanode exhibited great improvement in the photocurrent response compared with single  $\text{BiVO}_4$

and bare  $\text{WO}_3$  photoanodes. The partial replacement of  $\text{V}^{5+}$  sites by  $\text{Mo}^{6+}$  in  $\text{BiVO}_4$  can change the crystal symmetry of  $\text{BiVO}_4$  and introduce some polarons, both of which are beneficial for a higher charge carrier concentration, consequently improving the charge-transport capacity of the  $\text{BiVO}_4$  layer [45]. Therefore, the further enhanced PEC performance of the  $\text{WO}_3/\text{Mo-BiVO}_4$  photoanode can be attributed to the more efficient charge-transport capacity of the Mo-doped  $\text{BiVO}_4$  layer, which facilitates the separation of electron/hole pairs in the  $\text{BiVO}_4$  layer. The charge transfer capacity of the Co-Pi/ $\text{WO}_3/\text{Mo-BiVO}_4$  photoanode for water splitting is further enhanced because the Co-Pi co-catalyst facilitates the oxygen evolution reaction at the photoelectrode/electrolyte interface [32]. This progressive design maximizes the benefits of the  $\text{BiVO}_4$  and  $\text{WO}_3$  photoanode materials for efficient PEC applications.

#### 4. Conclusions

In conclusion, we demonstrated a facile, controllable, cost-effective method based on the reaction of bismuth nitrate with peroxovanadate on  $\text{WO}_3$  nanoplate films to fabricate undoped and Mo-doped  $\text{BiVO}_4/\text{WO}_3$  photoanodes for potentially efficient PEC water splitting and degradation of organic pollutants. The deposition amount of  $\text{BiVO}_4$  as well as the doping level could be tailored by tuning the growth conditions. The optimized number of spin-coating cycles and doping amount of Mo were 15 and 2 atomic%, respectively. Compared with conventional DA methods, the  $\text{WO}_3/\text{BiVO}_4$  photoanodes prepared in the present study should possess fewer nanostructural defects because this method avoids the repeated heating-cooling process used in DA methods, thus eliminating the possible negative effects on  $\text{WO}_3$  substrates. Specifically, an optimized Co-Pi/ $\text{WO}_3/\text{Mo-BiVO}_4$  photoanode showed a water splitting current density of  $5.24 \text{ mA cm}^{-2}$  with IPCE values

higher than 70% in the range of 350–450 nm and achieved stoichiometric H<sub>2</sub> and O<sub>2</sub> evolution with a H<sub>2</sub> generation rate of 94.7 μmol cm<sup>-2</sup> h<sup>-1</sup>. Furthermore, the WO<sub>3</sub>/Mo-BiVO<sub>4</sub> photoanode exhibited efficient performance in PEC degradation of organic pollutants with rate constants of 0.683, ~0.385, and ~1.05 h<sup>-1</sup> for tetracycline hydrochloride, phenol, and Congo red, respectively. This work demonstrates an efficient alternative method to prepare WO<sub>3</sub>/BiVO<sub>4</sub> photoanodes for potentially cost-effective and efficient PEC applications.

## Acknowledgements

The authors would like to acknowledge the National Nature Science Foundation of China (No. 21576162, No. 51578332, No. 21507085) and Shanghai Yangfan Program (14YF1401500) for financial support.

## Appendix A. Supplementary data

Supplementary data associated with this article can be found, in the online version, at <http://dx.doi.org/10.1016/j.apcatb.2017.05.072>.

## References

- [1] A. Fujishima, K. Honda, *Nature* 238 (1972) 37–38.
- [2] X. Chen, S. Shen, L. Guo, S.S. Mao, *Chem. Rev.* 110 (2010) 6503.
- [3] J. Bai, B. Zhou, *Chem. Rev.* 114 (2014) 10131–10176.
- [4] D.A. Wheeler, G. Wang, Y. Ling, Y. Li, J.Z. Zhang, *Energy Environ. Sci.* 5 (2012) 6682–6702.
- [5] G. Wang, Y. Ling, D.A. Wheeler, K.E.N. George, K. Horsley, C. Heske, J.Z. Zhang, Y. Li, *Nano Lett.* 11 (2011) 3503–3509.
- [6] R. Wang, J. Bai, Y. Li, Q. Zeng, J. Li, B. Zhou, *Nano-Micro Lett.* 9 (2017) 14.
- [7] X. Chen, Z. Zhang, L. Chi, A.K. Nair, W. Shangguan, Z. Jiang, *Nano-Micro Lett.* 8 (2016) 1–12.
- [8] J. Yang, X. Zhang, H. Liu, C. Wang, S. Liu, P. Sun, L. Wang, Y. Liu, *Catal. Today* 201 (2013) 195–202.
- [9] Q. Zeng, J. Bai, J. Li, Y. Li, X. Li, B. Zhou, *Nano Energy* 9 (2014) 152–160.
- [10] X. Chen, L. Liu, P.Y. Yu, S.S. Mao, *Science* 331 (2011) 746–750.
- [11] Q. Zheng, B. Zhou, J. Bai, L. Li, Z. Jin, J. Zhang, J. Li, Y. Liu, W. Cai, X. Zhu, *Adv. Mater.* 20 (2008) 1044–1049.
- [12] D. Wang, X. Zhang, P. Sun, S. Lu, L. Wang, Y. Wei, Y. Liu, *Int. J. Hydrogen Energy* 39 (2014) 16212–16219.
- [13] O.F. Lopesa, K.T.G. Carvalho, A.E. Nogueira, W.A. Caeu Ribeiro Jr., *Appl. Catal. B: Environ.* 188 (2016) 87–97.
- [14] Q. Jia, K. Iwashina, A. Kudo, P. Natl, *Acad. Sci. U. S. A.* 109 (2012) 11564–11569.
- [15] S.J. Hong, S. Lee, J.S. Jang, J.S. Lee, *Energy Environ. Sci.* 4 (2011) 1781–1787.
- [16] P. Chatchai, Y. Murakami, S. Kishioka, A.Y. Nosaka, Y. Nosaka, *Electrochim. Acta* 54 (2009) 1147–1152.
- [17] L. Xia, J. Bai, J. Li, Q. Zeng, X. Li, B. Zhou, *Appl. Catal. B: Environ.* 183 (2016) 224–230.
- [18] X. Shi, K. Zhang, K. Shin, M. Ma, J. Kwon, I.T. Choi, J.K. Kim, H.K. Kim, D.H. Wang, J.H. Park, *Nano Energy* 13 (2015) 182–191.
- [19] S.Y. Chae, H. Jung, H.S. Jeon, B.K. Min, Y.J. Hwang, O.-S. Joo, *J. Mater. Chem. A* 2 (2014) 11408–11416.
- [20] J. Su, L. Guo, N. Bao, C.A. Grimes, *Nano Lett.* 11 (2011) 1928–1933.
- [21] P.M. Rao, L. Cai, C. Liu, I.S. Cho, C.H. Lee, J.M. Weisse, P. Yang, X. Zheng, *Nano Lett.* 14 (2014) 1099–1105.
- [22] S. Kosar, Y. Pihosh, I. Turkevych, K. Mawatari, J. Uemura, Y. Kazoe, K. Makita, T. Sugaya, T. Matsui, D. Fujita, M. Tosa, Y.M. Struk, M. Kondo, T. Kitamori, *Jpn. J. Appl. Phys.* 55 (2016) 04ES01.
- [23] Y. Pihosh, I. Turkevych, K. Mawatari, J. Uemura, Y. Kazoe, S. Kosar, K. Makita, T. Sugaya, T. Matsui, D. Fujita, M. Tosa, M. Kondo, T. Kitamori, *Sci. Rep.* 5 (2015) 11141.
- [24] Q. Zeng, J. Li, J. Bai, X. Li, L. Xia, B. Zhou, *Appl. Catal. B: Environ.* 202 (2017) 388–396.
- [25] S. Tokunaga, H. Kato, A. Kudo, *Chem. Mater.* 13 (2001) 4624–4628.
- [26] M. Sadakane, K. Sasaki, H. Kunioku, B. Ohtani, R. Abe, W. Ueda, *J. Mater. Chem.* 20 (2010) 1811–1818.
- [27] Y. Zhang, D. Wang, X. Zhang, Y. Chen, L. Kong, P. Chen, Y. Wang, C. Wang, L. Wang, Y. Liu, *Electrochim. Acta* 195 (2016) 51–58.
- [28] W.F. Yao, H.D. Iwai, J.H. Ye, *Dalton Trans.* 11 (2008) 1426.
- [29] S.P. Berglund, A.J.E. Rettie, S. Hoang, C.B. Mullins, *Phys. Chem. Chem. Phys.* 14 (2012) 7065–7075.
- [30] G. Wang, Y. Ling, H. Wang, X. Yang, C. Wang, J.Z. Zhang, Y. Li, *Energy Environ. Sci.* 5 (2012) 6180–6187.
- [31] L. Ge, C. Han, X. Xiao, L. Guo, *Appl. Catal. B: Environ.* 142–143 (2013) 414–422.
- [32] S. Hernández, G. Gerardi, K. Bejtka, A. Fina, N. Russo, *Appl. Catal. B: Environ.* 190 (2016) 66–74.
- [33] T. Jin, P. Diao, Q. Wu, D. Xu, D. Hu, Y. Xie, M. Zhang, *Appl. Catal. B: Environ.* 148–149 (2014) 304–310.
- [34] X. Zhang, F. Liu, Q.-L. Huang, G. Zhou, Z.-S. Wang, *J. Phys. Chem. C* 115 (2011) 12665–12671.
- [35] J. Kruger, R. Plass, M. Grätzel, P.J. Cameron, L.M. Peter, *J. Phys. Chem. B* 107 (2003) 7536–7539.
- [36] Q. Zeng, J. Bai, J. Li, L. Xia, K. Huang, X. Li, B. Zhou, *J. Mater. Chem. A* 3 (2015) 4345–4353.
- [37] G. Mamba, A.K. Mishra, *Appl. Catal. B: Environ.* 198 (2016) 347–377.
- [38] H. Zhang, L. Zhao, F. Geng, L.-H. Guo, B. Wan, Y. Yang, *Appl. Catal. B: Environ.* 180 (2016) 656–662.
- [39] Q. Chen, J. Li, X. Li, K. Huang, B. Zhou, W. Cai, W. Shangguan, *Environ. Sci. Technol.* 46 (2012) 11451–11458.
- [40] L.V.C. Lima, M. Rodriguez, V.A.A. Freitas, T.E. Souza, A.E.H. Machado, A.O.T. Patrocínio, J.D. Fabris, L.C.A. Oliveira, M.C. Pereira, *Appl. Catal. B: Environ.* 165 (2015) 579–588.
- [41] Y. Chang, K. Yu, C. Zhang, R. Li, P. Zhao, L.-L. Lou, S. Liu, *Appl. Catal. B: Environ.* 176–177 (2015) 363–373.
- [42] F.F. Abdi, T.J. Savenije, M.M. May, B. Dam, R. Krol, *J. Phys. Chem. Lett.* 4 (2013) 2752–2757.
- [43] T.W. Kim, K.S. Choi, *Science* 343 (2014) 990–994.
- [44] D. Eisenberg, H.S. Ahn, A.J. Bard, *J. Am. Chem. Soc.* 136 (2014) 14011–14014.
- [45] Q. Wang, T. Hisatomi, Q. Jia, H. Tokudome, M. Zhong, C. Wang, Z. Pan, T. Takata, M. Nakabayashi, N. Shibata, Y. Li, I.D. Sharp, A. Kudo, T. Yamada, K. Domen, *Nat. Mater.* 15 (2016) 4589.
- [46] S.S. Kalanur, Y.J. Hwang, S.Y. Chae, O.-S. Joo, *J. Mater. Chem. A* 1 (2013) 3479–3488.
- [47] B. Zhang, F. Wang, C. Zhu, Q. Li, J. Song, M. Zheng, L. Ma, W. Shen, *Nano-Micro Lett.* 8 (2016) 137–142.